Coherent mode coupling in highly efficient top-emitting OLEDs on periodically corrugated substrates

Tobias Schwab,[1,2,*] **Cornelius Fuchs,**[1,2] **Reinhard Scholz,**[2] **Alexander Zakhidov,**[3] **Karl Leo,**[2] **and Malte C. Gather**[2,4]

[1] *These authors contributed equally to this work.*
[2] *Institut für Angewandte Photophysik, Technische Universität Dresden, 01062 Dresden, Germany*
[3] *Fraunhofer COMEDD, Maria Reiche Straße 2, 01109 Dresden, Germany*
[4] *SUPA, School of Physics and Astronomy, University of St Andrews, St Andrews, KY16 9SS, UK*
[*] *tobias.schwab@iapp.de*

Abstract: Bragg scattering at one-dimensional corrugated substrates allows to improve the light outcoupling from top-emitting organic light-emitting diodes (OLEDs). The OLEDs rely on a highly efficient phosphorescent pin stack and contain metal electrodes that introduce pronounced microcavity effects. A corrugated photoresist layer underneath the bottom electrode introduces light scattering. Compared to optically optimized reference OLEDs without the corrugated substrate, the corrugation increases light outcoupling efficiency but does not adversely affect the electrical properties of the devices. The external quantum efficiency (EQE) is increased from 15 % for an optimized planar layer structure to 17.5 % for a corrugated OLED with a grating period of 1.0 μm and a modulation depth of about 70 nm. Detailed analysis and optical modeling of the angular resolved emission spectra of the OLEDs provide evidence for Bragg scattering of waveguided and surface plasmon modes that are normally confined within the OLED stack into the air-cone. We observe constructive and destructive interference between these scattered modes and the radiative cavity mode. This interference is quantitatively described by a complex summation of Lorentz-like resonances.

OCIS codes: (230.3670) Light-emitting diodes; (230.4000) Microstructure fabrication; (160.4890) Organic materials; (050.2770) Gratings.

References and links

1. S. Reineke, F. Lindner, G. Schwartz, N. Seidler, K. Walzer, B. Lüssem, and K. Leo, "White organic light-emitting diodes with fluorescent tube efficiency." Nature **459**, 234–238 (2009).
2. Z. B. Wang, M. G. Helander, J. Qiu, D. P. Puzzo, M. T. Greiner, Z. M. Hudson, S. Wang, Z. W. Liu, and Z. H. Lu, "Unlocking the full potential of organic light-emitting diodes on flexible plastic," Nat. Photonics **5**, 753–757 (2011).
3. S. Hofmann, M. Thomschke, P. Freitag, M. Furno, B. Lüssem, and K. Leo, "Top-emitting organic light-emitting diodes: Influence of cavity design," Appl. Phys. Lett. **97**, 253308 (2010).
4. T. Schwab, S. Schubert, S. Hofmann, M. Fröbel, C. Fuchs, M. Thomschke, L. Müller-Meskamp, K. Leo, and M. C. Gather, "Highly efficient and color stable inverted white top-emitting OLEDs with ultra-thin wetting layer top electrodes," Adv. Opt. Mater. **1**, 707–713 (2013).

#197952 - $15.00 USD Received 18 Sep 2013; revised 28 Nov 2013; accepted 19 Dec 2013; published 25 Mar 2014

5. T. Schwab, S. Schubert, L. Müller-Meskamp, K. Leo, and M. C. Gather, "Eliminating Micro-Cavity Effects in White Top-Emitting OLEDs by Ultra-Thin Metallic Top Electrodes," Adv. Opt. Mater. **1**, 921–925 (2013).
6. C. Adachi, M. A. Baldo, M. E. Thompson, and S. R. Forrest, "Nearly 100% internal phosphorescence efficiency in an organic light-emitting device," J. Appl. Phys. **90**, 5048–5051 (2001).
7. B. J. Matterson, J. M. Lupton, a. F. Safonov, M. G. Salt, W. L. Barnes, and I. D. W. Samuel, "Increased efficiency and controlled light output from a microstructured light-emitting diode," Adv. Mater. **13**, 123–127 (2001).
8. S. Wedge and W. Barnes, "Surface plasmon-polariton mediated light emission through thin metal films." Opt. Express **12**, 3673–3685 (2004).
9. R. Meerheim, M. Furno, S. Hofmann, B. Lüssem, and K. Leo, "Quantification of energy loss mechanisms in organic light-emitting diodes," Appl. Phys. Lett. **97**, 253305 (2010).
10. S. Moeller and S. R. Forrest, "Improved light out-coupling in organic light emitting diodes employing ordered microlens arrays," J. Appl. Phys. **91**, 3324–3327 (2002).
11. H. Greiner, "Light extraction from organic light emitting diode substrates: Simulation and experiment," Jpn. J. Appl. Phys. **46**, 4125–4137 (2007).
12. T. C. Rosenow, M. Furno, S. Reineke, S. Olthof, B. Lüssem, and K. Leo, "Highly efficient white organic light-emitting diodes based on fluorescent blue emitters," J. Appl. Phys. **108**, 113113 (2010).
13. N. Patel, S. Cina, and J. Burroughes, "High-efficiency organic light-emitting diodes," IEEE J. Sel. Top. Quantum Electron. **8**, 346–361 (2002).
14. K. Saxena, V. Jain, and D. S. Mehta, "A review on the light extraction techniques in organic electroluminescent devices," Opt. Mater. **32**, 221–233 (2009).
15. B. J. Scholz, J. Frischeisen, A. Jaeger, D. S. Setz, T. C. Reusch, and W. Brütting, "Extraction of surface plasmons in organic light-emitting diodes via high-index coupling," Opt. Express **20**, A205–A212 (2012).
16. M. Thomschke, S. Reineke, B. Lüssem, and K. Leo, "Highly efficient white top-emitting organic light-emitting diodes comprising laminated microlens films." Nano Letters **12**, 424–428 (2012).
17. T. W. Canzler, S. Murano, D. Pavicic, O. Fadhel, C. Rothe, A. Haldi, M. Hofmann, and Q. Huang, "Efficiency enhancement in white PIN OLEDs by simple internal outcoupling methods," SID Symp. Dig. Tech. Papers **42**, 975–978 (2011).
18. Z. Wang, Z. Chen, L. Xiao, and Q. Gong, "Enhancement of top emission for organic light-emitting diode via scattering surface plasmons by nano-aggregated outcoupling layer," Org. Electron. **10**, 341–345 (2009).
19. S.-Y. Nien, N.-F. Chiu, Y.-H. Ho, J.-H. Lee, C.-W. Lin, K.-C. Wu, C.-K. Lee, J.-R. Lin, M.-K. Wei, and T.-L. Chiu, "Directional photoluminescence enhancement of organic emitters via surface plasmon coupling," Appl. Phys. Lett. **94**, 103304 (2009).
20. J. Frischeisen, Q. Niu, A. Abdellah, J. B. Kinzel, R. Gehlhaar, G. Scarpa, C. Adachi, P. Lugli, and W. Brütting, "Light extraction from surface plasmons and waveguide modes in an organic light-emitting layer by nanoimprinted gratings." Opt. Express **19**, A7–A19 (2011).
21. J. M. Ziebarth, A. K. Saafir, S. Fan, and M. D. McGehee, "Extracting light from polymer light-emitting diodes using stamped Bragg gratings," Adv. Funct. Mater. **14**, 451–456 (2004).
22. Y. Bai, J. Feng, Y.-F. Liu, J.-F. Song, J. Simonen, Y. Jin, Q.-D. Chen, J. Zi, and H.-B. Sun, "Outcoupling of trapped optical modes in organic light-emitting devices with one-step fabricated periodic corrugation by laser ablation," Org. Electron. **12**, 1927–1935 (2011).
23. Y.-G. Bi, J. Feng, Y.-F. Li, Y. Jin, Y.-F. Liu, Q.-D. Chen, and H.-B. Sun, "Enhanced efficiency of organic light-emitting devices with metallic electrodes by integrating periodically corrugated structure," Appl. Phys. Lett. **100**, 053304 (2012).
24. T. Bocksrocker, J. B. Preinfalk, J. Asche-Tauscher, A. Pargner, C. Eschenbaum, F. Maier-Flaig, and U. Lemmer, "White organic light emitting diodes with enhanced internal and external outcoupling for ultra-efficient light extraction and Lambertian emission." Opt. Express **20**, A932–A940 (2012).
25. Y. Jin, J. Feng, X.-L. Zhang, Y.-G. Bi, Y. Bai, L. Chen, T. Lan, Y.-F. Liu, Q.-D. Chen, and H.-B. Sun, "Solving efficiency-stability tradeoff in top-emitting organic light-emitting devices by employing periodically corrugated metallic cathode." Adv. Mater. **24**, 1187–1191 (2012).
26. U. Geyer, J. Hauss, B. Riedel, S. Gleiss, U. Lemmer, and M. Gerken, "Large-scale patterning of indium tin oxide electrodes for guided mode extraction from organic light-emitting diodes," J. Appl. Phys. **104**, 093111 (2008).
27. B. Riedel, J. Hauss, U. Geyer, J. Guetlein, U. Lemmer, and M. Gerken, "Enhancing outcoupling efficiency of indium-tin-oxide-free organic light-emitting diodes via nanostructured high index layers," Appl. Phys. Lett. **96**, 243302 (2010).
28. C. Fuchs, T. Schwab, T. Roch, S. Eckardt, A. Lasagni, S. Hofmann, B. Lüssem, L. Müller-Meskamp, K. Leo, M. C. Gather, and R. Scholz, "Quantitative allocation of Bragg scattering effects in highly efficient OLEDs fabricated on periodically corrugated substrates," Opt. Express **21**, 16319–16330 (2013).
29. M. Pfeiffer, "Doped organic semiconductors: Physics and application in light emitting diodes," Org. Electron. **4**, 89–103 (2003).
30. Q. Huang, K. Walzer, M. Pfeiffer, K. Leo, and M. Hofmann, "Performance improvement of top-emitting organic light-emitting diodes by an organic capping layer: An experimental study," J. Appl. Phys. **100**, 064507 (2006).
31. M. Furno, R. Meerheim, S. Hofmann, B. Lüssem, and K. Leo, "Efficiency and rate of spontaneous emission in

#197952 - $15.00 USD Received 18 Sep 2013; revised 28 Nov 2013; accepted 19 Dec 2013; published 25 Mar 2014

organic electroluminescent devices," Phys. Rev. B **85**, 115205 (2012).
32. M. Thomschke, R. Nitsche, M. Furno, and K. Leo, "Optimized efficiency and angular emission characteristics of white top-emitting organic electroluminescent diodes," Appl. Phys. Lett. **94**, 083303 (2009).
33. H. Rigneault, F. Lemarchand, and A. Sentenac, "Dipole radiation into grating structures," J. Opt. Soc. Am. A **17**, 1048–1058 (2000).
34. J. Hauss, T. Bocksrocker, B. Riedel, U. Lemmer, and M. Gerken, "On the interplay of waveguide modes and leaky modes in corrugated OLEDs," Opt. Express **19**, A851–A858 (2011).

1. Introduction

Future applications of organic light-emitting diodes (OLEDs) for general illumination and displays require efficient [1], flexible [2], large area, low-cost, and versatile device architectures. Top-emitting OLEDs are very interesting candidates in this context as they combine high efficiency and compatibility with pre-processed backplane driver electronics and roll-to-roll manufacturing schemes on flexible, opaque substrates, such as metal foils. It has been shown that single color top-emitting OLEDs can easily surpass the efficiency of their bottom-emitting counterparts [3] and that white top-emitting can at least achieve similar efficiency [4, 5].

However, even for OLEDs with an internal quantum efficiency of nearly 100 % [6], the maximum external quantum efficiency achieved up to now for a planar device layout without light outcoupling structure is only approximately 30 % [3]. This results from the trapping of the majority of generated light within the device, e.g. as bound organic or surface plasmon polariton (SPP) modes [7–9]. Several approaches have been reported to extract trapped light from these modes in bottom-emitting OLEDs, including the use of macroscopic outcoupling structures like microlens arrays [10, 11] or pyramidal structures [1, 12], index matching half-spheres [12, 13], and / or high-index substrates [14, 15]. Recently, Thomschke *et al.* have demonstrated that a micro-lens foil can also be laminated onto the top-contact of top-emitting OLEDs to extract trapped light modes from these devices [16]. However, it is still not clear whether top-emitting OLEDs can benefit from such approaches on an industrial scale due to the technical challenges involved in attaching such outcoupling structures onto the semitransparent top contact of the device without damaging the layers underneath.

Furthermore, approaches based on organic scattering layers that are inserted either between the electrodes or on the top electrode have been reported and may prove to be a versatile and generally applicable method to increase OLED efficiency [17, 18]. For an application in commercial products, scattering by randomly distributed particles seems adequate. However, details on the physics of the scattering process are obscured by this form of scattering. By contrast, Bragg scattering of the bound modes by periodic structures allows a more detailed investigation of the scattering mechanism. In future devices, tuning period and amplitude of the corrugation may also enable more efficient and more controlled light extraction than random scattering.

There is already some evidence that periodic outcoupling structures can achieve enhancement factors comparable to the enhancement obtained with random scatterers. For instance, optical excitation of single emissive layers on periodically corrugated substrates showed strong emission enhancements by up to a factor of four [19]. Extraction of optical energy from waveguided modes and surface plasmon modes was found to enhance the intensity of emission. While large enhancement factors were achieved for optical excitation, electrical driving of these devices was not achieved [19, 20]. Investigations on bottom-emitting OLEDs incorporating periodic gratings showed that the emission can be enhanced by up to a factor of 2.0 compared to a non-corrugated reference device [21–24]. Electrically operating top-emitting OLEDs on corrugated substrates have been shown by Jin *et al.* [25] in 2012, but the overall device performance still remains quite low. For the corrugated OLEDs reported so far, the electrical device characteristics differ significantly from those of planar reference devices. This suggests that not only the light extraction efficiency but also the internal quantum efficiency is affected

#197952 - $15.00 USD Received 18 Sep 2013; revised 28 Nov 2013; accepted 19 Dec 2013; published 25 Mar 2014

by the corrugation [21, 22, 26, 27]. Therefore, the observed efficiency enhancements might be caused by enhanced internal quantum efficiency and not exclusively by improved light outcoupling. Very recently, we showed that introducing a corrugated transparent anode of Al:ZnO can yield an efficiency enhancement of 30 % with respect to an optically optimized, non-corrugated state-of-the-art bottom-emitting OLED without affecting the electrical characteristics of the device [28].

Here, we report on a method to introduce a periodically corrugated photoresist layer with a characteristic length scale in the μm-range directly underneath the bottom contact of top-emitting OLEDs. We investigate different corrugation periods and heights and find that such a grating-type structure can lead to a significant enhancement in device efficiency with respect to a non-corrugated, optically optimized phosphorescent top-emitting reference device. At the same time, the corrugation introduced by our method does not adversely affect the electrical device characteristics. The EQE increases from 15 % for an optimized planar OLED to 17.5 % for the corrugated device.

The coupling between vertical microcavity modes and scattering at the corrugated photoresist structure leads to additional phenomena in top-emitting OLEDs, not observed in our previous studies on bottom-emitting OLEDs comprising a corrugated transparent anode [28]. Angle resolved emission spectroscopy of our top-emitting OLEDs reveals a series of sharp and pronounced spectral features for the corrugated OLEDs that are not present in a planar reference device. By careful comparison with data from optical modeling, we show that the efficiency enhancement is due to Bragg scattering of the waveguided and SPP modes at the corrugated layer. In planar devices, these modes are trapped within the active region of the OLED but can be extracted from the device by the scattering process. For devices with a small corrugation period and a larger corrugation height, the interaction of Bragg scattered modes and the original radiative states becomes more complex and constructive as well as destructive interference between modes is observed. We show that this phenomenon can be described with good accuracy by fitting the experimental data with the complex sum of up to five Lorentz-like resonances.

In the following section, we explain the fabrication and characterization procedure used in this study. Then, we introduce and discuss the results of electrical and optical measurements on these devices and compare their performance. To explain the efficiency enhancements observed for devices on corrugated substrates, we perform a theoretical analysis of the experimentally determined radiation patterns of the OLEDs.

2. Experimental

The corrugated structure in the OLEDs is obtained by depositing the organic materials and the metallic contacts of the device onto a corrugated photoresist layer. The corrugated layer comprises a photo-lithographically structured layer of the negative photoresist AZ nLOF 2020 (MicroChemicals). The resist is first spin coated on pre-cleaned, planar glass substrates (size, 2.5 cm $\times$ 2.5 cm) and pre-baked for one minute at 110°C. Afterwards the resist is exposed to UV radiation from a high-pressure mercury lamp through a contact mask with alternating transparent and opaque stripes of different period. The exposure is followed by another one minute baking step at 110°C. A tetra-methylammoniumhydroxid (TMAH) based developer (MicroChemicals) was used to remove the non-exposed photoresist, leaving the bare corrugated photoresist on the glass substrate. Atomic force microscopy scans (CombiScope 1000, AIST-NT) show that this process yields very uniform one dimensional gratings (Figs. 1(b) and 1(c)).

#197952 - $15.00 USD Received 18 Sep 2013; revised 28 Nov 2013; accepted 19 Dec 2013; published 25 Mar 2014

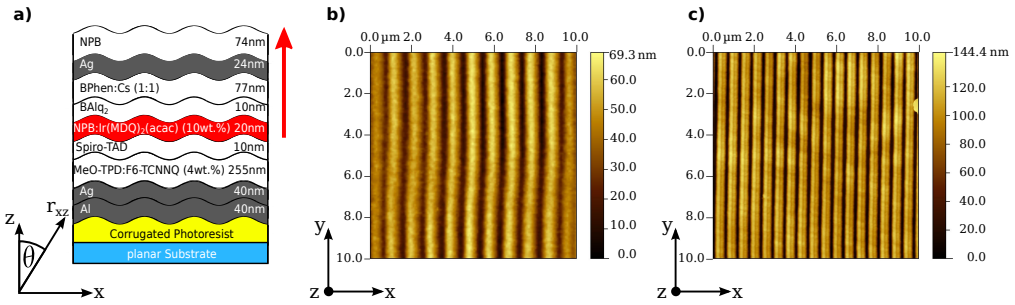

Fig. 1. (a) Schematic illustration of the phosphorescent top-emitting OLEDs investigated in this study, comprising a corrugated photoresist layer directly underneath the double-layer bottom contact of the device. The red arrow marks the direction of emission. (b),(c) Atomic force microscopy data of the lithographically structured photoresist layers prior to deposition of the OLED stack for layers with a corrugation period of 1.0 μm (b) and 0.6 μm (c).

In the following, measurements for samples with two different grating periods are discussed. For a larger grating period of $\Lambda = 1.0\,\mu$m, the corrugation depth was $h = 69$ nm, giving an aspect ratio of 0.07 (Fig. 1(b)). For the smaller grating, the nominal period was $\Lambda = 0.6\,\mu$m and the corrugation depth was h = 144 nm, corresponding to an aspect ratio $r_h = h/\Lambda$ of 0.24 (Fig. 1(c)). The nominal grating periods represent the design value of the contact mask and are used to refer to the different samples throughout the text.

The stack architecture of the OLEDs used in this study is illustrated in Fig. 1(a). The stack is based on the *pin*-concept and uses doped charge transport layers, a pair of charge and exciton blocking layers and an emissive layer at the center of the device [29]. The opaque bottom contact is composed of 40 nm of aluminum (**Al**) and 40 nm of silver (**Ag**). A 255 nm-thick hole transport layer (HTL) is formed by co-evaporation of N,N,N',N'-tetrakis(4-methoxyphenyl)-benzidine (**MeO-TPD**) as matrix doped with 4 wt.% of 2,2'-(perfluoronaphthalene-2,6-diylidene)dimalononitrile (**F6-TCNNQ**). The thick HTL is chosen to prevent electrical shorts that might otherwise occur due to the corrugated photoresist layer underneath. The HTL is followed by the electron blocking layer (EBL) consisting of 2,2',7,7'-tetrakis-(N,N-diphenylamino)-9,9'-spirobifluorene (**Spiro-TAD**). For the emissive layer, we used the phosphorescent red-emitting Iridium(III)bis(2-methyldibenzo-[f,h]chinoxalin)(acetylacetonate) (**Ir(MDQ)$_2$(acac)**) doped at 10 wt.% into N,N'-Di(naphthalen-1-yl)-N,N'-diphenyl-benzidine (**NPB**). The hole blocking layer (HBL) is formed by Aluminum (III) bis(2-methyl-8-quninolinato)-4-phenylphenolate (**BAlq$_2$**) and the electron transport layer (ETL) consists of 4,7-diphenyl-1,10-phenanthroline (**BPhen**) doped with cesium (**Cs**) (ETL). The Cs-doping level is adjusted to obtain a conductivity of 10^{-5} S/cm. The cathode contact is formed by a semitransparent 24 nm thin silver layer, enabling light emission through this top contact. The final layer of the device is formed by an electrically passive, organic capping layer consisting of **NPB**. Such a capping layer is known to enhance the light outcoupling efficiency of planar top-emitting OLEDs [30]. All the layers were deposited by thermal evaporation at a base pressure of 10^{-7} to 10^{-8} mbar using a single chamber high vacuum tool (Kurt J. Lesker Company). After preparation, the OLEDs are encapsulated under nitrogen atmosphere with a glass lid.

The current-voltage-luminescence characteristics of the OLEDs were measured using a Source Measure Unit 2400 (Keithley) and a photo-diode. The spectral radiant intensity in normal direction was recorded with a CAS140 spectrometer (Instrument Systems GmbH). Angu-

#197952 - $15.00 USD Received 18 Sep 2013; revised 28 Nov 2013; accepted 19 Dec 2013; published 25 Mar 2014

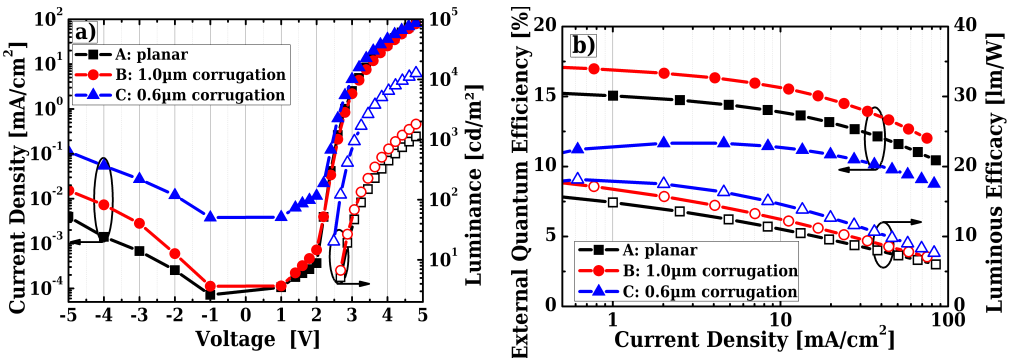

Fig. 2. (a) Current-voltage-luminance characteristics in forward direction and (b) angular corrected current-efficiency characteristics of the planar and corrugated top-emitting OLEDs. The nominal period of corrugation was $\Lambda_{B,\mathrm{mask}} = 1.0\,\mu$m and $\Lambda_{C,\mathrm{mask}} = 0.6\,\mu$m, respectively. The grating structure improved the device efficiency even though the electrical performance of all devices remained comparable.

lar dependent measurements of the OLED emission spectra were performed in 1° steps with a custom-built spectro-goniometer comprising a rotational sample stage, a USB-4000 mini spectrometer (Ocean Optics), and a polarization filter (Thorlabs) to select the polarization. Each spectrum was recorded at a constant applied current of 1 mA (corresponding to a current density of 14.8 mA/cm^2). The angular resolved emission spectra were used to calculate the EQE and the luminous efficacy (LE) of the devices and to analyze scattering at the corrugated structures in detail.

3. Results and discussion

In the following, we discuss results on three different devices: Device A is a planar reference OLED. Device B comprises a grating with a nominal period of $\Lambda_{B,\mathrm{mask}} = 1.0\,\mu$m. The third device (Device C) had a nominal lattice constant of $\Lambda_{C,\mathrm{mask}} = 0.6\,\mu$m. The thickness of all layers was identical for all devices. The thickness of the HTL was tuned such that the planar reference device operates in the second efficiency maximum [31]. The thickness of the other organic layers in this device was optimized for maximum outcoupling efficiency.

3.1. Performance of top-emitting OLEDs on periodically corrugated substrates

As can be seen from Fig. 2(a), all devices show comparable current-voltage characteristics under forward bias. The turn-on voltages for all devices are below 2.5 V, which is close to the thermal equilibrium energy for generating a photon on the emitting Ir(MDQ)$_2$(acac) molecules. These low turn-on voltages are possible due to the use of doped charge transport layers that virtually eliminate the influence of charge injection barriers and voltage drop across the relatively thick charge transport layers. Under reverse bias, the leakage current is somewhat higher in the corrugated top-emitting OLEDs than in the planar reference, but remains at an acceptable level. We attribute the absence of severe leakage in the devices with sub-μm grating structures to the fact that our corrugated photoresist structures do not contain any sharp spikes that could lead to defects in the organic layers. Maintaining electrical stability when introducing the corrugation is a key requirement to achieve stable, long-term device operation and high efficiencies. For the corrugated top-emitting devices with 0.6 μm corrugation period, the forward luminance in Fig. 2(a) is significantly enhanced with respect to the planar reference. By comparison, the forward luminance is relatively unaffected by the 1.0 μm corrugation.

#197952 - $15.00 USD Received 18 Sep 2013; revised 28 Nov 2013; accepted 19 Dec 2013; published 25 Mar 2014

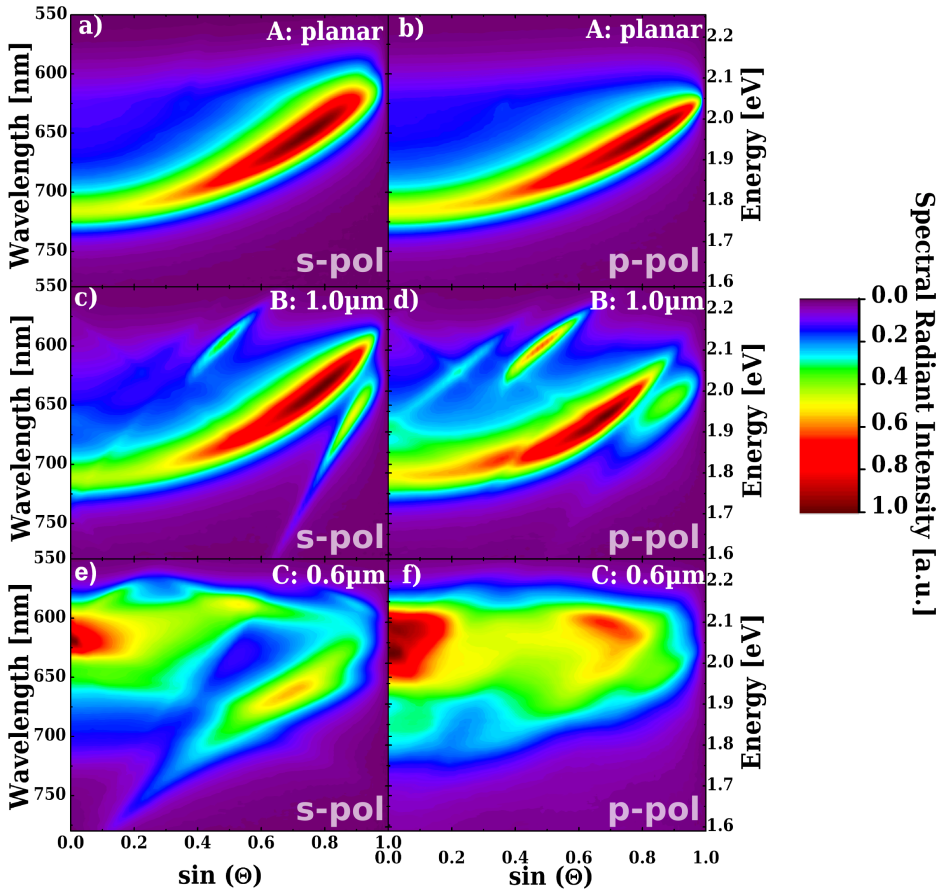

Fig. 3. Measured angular dependent emission spectra for planar reference Device A in s-polarization (a) and p-polarization (b), corrugated OLEDs Device B (c) and (d), and Device C (e) and (f). All spectra recorded under electrical operation with constant current driving at 14.8 mA/cm^2.

The EQE and the luminous efficacy for all devices are shown in Fig. 2(b). The planar top-emitting OLED (Device A) reaches 15 % EQE at low current density. This value is comparable to literature reports on the most efficient single-color top-emitting OLEDs operating in the second optical maximum [3]. Compared to the planar reference, Device B ($\Lambda_{B,\mathrm{mask}} = 1.0\,\mu$m) shows an enhanced EQE over the entire current range investigated. At a current density of 1 mA/cm^2, the EQE is increased from 15.0 % for Device A to 17.0 % for Device B. This represents an enhancement of 13 % with respect to an already highly efficient top-emitting OLED. By contrast, for the device with the shorter corrugation period (Device C, $\Lambda_{C,\mathrm{mask}} = 0.6\,\mu$m), the EQE is reduced compared to the reference although the forward luminance for Device C was found to be by a factor of 11.3 higher than for Device A. The LE of both corrugated devices is higher than for Device A. Device A reaches a LE of 16.2 lm/W while Devices B and C both reach 18.4 lm/W LE at a current density of 1 mA/cm^2, corresponding to an increase of 13.5 %.

#197952 - $15.00 USD Received 18 Sep 2013; revised 28 Nov 2013; accepted 19 Dec 2013; published 25 Mar 2014

3.2. Mode analysis of top-emitting OLEDs on periodically corrugated substrates

In order to explain the efficiency enhancements observed for Devices B and C, we evaluate the angular resolved emission spectra. Figures. 3(a) and 3(b) show the measured emission spectra of the planar reference device for observation angles θ in the range of $\sin\theta$ between 0 and 1. The radiative cavity mode shows a parabolic dispersion shifting to the blue for higher emission angles [32]. The measured angular resolved emission spectra for the corrugated devices (B and C) are shown in Figs. 3(c)-3(f). A comparison to the planar device (A) shows that several new spectral features are introduced by the periodic grating. For Device B the radiative cavity mode is still very prominent, but additional modes are observed within the forward emission cone ($0 < \sin\theta < 1$). By contrast, Device C with the smaller corrugation period of 0.6 μm shows a quite different emission pattern with a strong emission peak in forward direction ($\sin\theta = 0$).

In our model, we describe the corrugated photoresist structure as a periodic perturbation to the optical microcavity of the OLED [28]. This allows us to estimate the angular position of additional features in the angular resolved emission spectra from the well-known Bragg scattering equation:

$$k_x = k_{x,\mathrm{int}} - m \cdot G. \tag{1}$$

Here, k_x is the in-plane wavenumber of outcoupled radiation, related to the emission angle θ and the wavenumber k_0 in air by $k_x/k_0 = \sin\theta$. This equation indicates that for sufficiently large reciprocal lattice numbers $G = 2\pi/\Lambda$ or sufficiently high scattering orders m, light that would normally be trapped within the device (i.e. with in-plane wavenumbers $k_{x,\mathrm{int}} > k_0$) can be partly outcoupled into air. According to Rigneault *et al.*, Eq. (1) adequately describes the situation in the OLED as long as the grating height is smaller than the optical thickness of the cavity, i.e. $h/d_{\mathrm{opt}} < 1$ [33]. This is fulfilled for Device B ($h_B/d_{\mathrm{opt}} = 0.16$) and Device C ($h_C/d_{\mathrm{opt}} = 0.33$). To analyze the scattering effects in Device B and C in detail, we first calculate the power dissipation spectrum for the planar device using a well-established transfer matrix and radiative dipole model [31]. The power dissipation spectrum describes the relative optical power emitted versus photon energy (or wavelength) and in-plane wavenumber k_x. In contrast to the measured angular resolved emission spectrum, the power dissipation spectrum can also be calculated for $k_{x,\mathrm{int}}/k_0 > 1$, i.e. for light that is trapped within the device. As the layer sequence and thickness is identical for Device A, B, and C and because the corrugation is described by a small perturbation to the planar microcavity, the dispersion of radiative, waveguided and SPP modes of Device A should also describe the situation in Devices B and C.

Figure 4 shows a superposition of the calculated power dissipation spectrum of Device A and the measured angular resolved emission spectrum of Device B (c.f. Figs. 3(c) and 3(d)). In the measured data, the emission angle θ is converted into the in-plane wavenumber k_x and the wavelength is converted to photon energy E for better visualization. The measured spectra cover the range from $k_x = 0$ to the air light line. The air light line corresponds to $E = \hbar c k_0$ or $k_x/k_0 = \sin\theta = 1$ and is shown as a dash-dotted line. Beyond the light line, Fig. 4 shows the calculated power dissipation spectrum. The dispersion relations of radiative, waveguided and SPP modes were extracted from the power dissipation spectrum and are shown as white dashed lines across the entire k_x range. The dispersion of the emissive mode agrees well with the strongest feature in the measured angular resolved emission spectra for both, the s- and the p-polarized case, indicating that our calculation is based on the correct layer thickness and optical constants of the materials involved. The waveguided modes propagate with approximately linear dispersion relations with refractive group indices $n_{\mathrm{g}} = \partial k_x/\partial k_0 =$ of 2.08 (WGs1) and 2.48 (WGs2) for the first and second waveguided mode in s-polarization, and 2.47 (WGp1) and 3.27 (WGp2) for p-polarization, respectively.

In the calculated p-polarized power dissipation spectrum shown in Fig. 4(b) we observe the dispersion relations of two SPP modes within the evanescent regime of the power dissipation

#197952 - $15.00 USD Received 18 Sep 2013; revised 28 Nov 2013; accepted 19 Dec 2013; published 25 Mar 2014

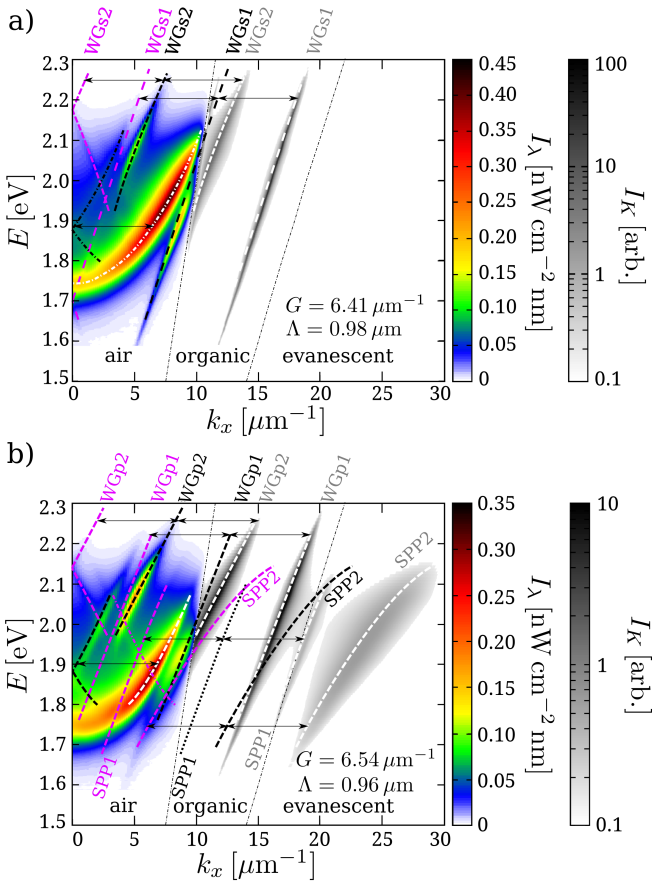

Fig. 4. Measured spectral radiant intensity (false color scale) of Device B (a) in s-polarization and (b) p-polarization, along with the simulated power dissipation spectra of a planar microcavity (grayscale) outside the experimentally accessible region. Air and organic light line (dash-dotted lines), expected position of the dispersion of the radiative mode and waveguided modes (white dashed lines) are also indicated. Bragg scattering of these modes leads to additional features in the emission spectrum (highlighted by black and purple dashed lines). Black arrows indicate the reciprocal lattice vector *G* and link the modes of the planar microcavity to modes arising from Bragg scattering.

#197952 - $15.00 USD Received 18 Sep 2013; revised 28 Nov 2013; accepted 19 Dec 2013; published 25 Mar 2014

spectra. The first one originates from the thick metallic bottom contact and propagates close to the organic light line with a refractive group index of 2.46 (SPP1). The second SPP mode is the coupled state of the two SPPs at the interfaces of the thin silver top contact. This mode shows a more non-linear dispersion far to the right of the organic light line. As the HTL thickness in our devices was chosen to form a second order optical microcavity, coupling to both SPP modes is weak. They are thus barely visible in the power dissipation spectra and scattering of these modes is not expected to be detectable.

Next, we attempt to assign the additional peaks in the measured angular resolved emission spectra of the corrugated device to Bragg scattered modes. For a lattice vector in the range of $G \approx 2\pi/\Lambda_{B,\mathrm{mask}}$, this is achieved when taking into account first and second order scattering of waveguided modes, and first order scattering of the radiative cavity mode. When leaving G as a free parameter, we find that the position of all additional peaks in the measured angular resolved emission spectra is best described for $G_{B,\mathrm{s-pol}} = 6.41\,\mu\mathrm{m}^{-1}$ for the s-polarized case and $G_{B,\mathrm{p-pol}} = 6.54\,\mu\mathrm{m}^{-1}$ for the p-polarized case, corresponding to a corrugation period of $\Lambda_{B,\mathrm{s-pol}} = 0.98\,\mu\mathrm{m}$ and $\Lambda_{B,\mathrm{p-pol}} = 0.96\,\mu\mathrm{m}$, respectively. This represents an excellent agreement to the nominal lattice period of $\Lambda_{B,\mathrm{mask}} = 1.0\,\mu\mathrm{m}$, where the residual deviation may arise from the uncertainty of the refractive indices of the various organic layers. As the electrical properties of Device B are similar to Device A, we conclude that the additional outcoupled radiation leads to the observed efficiency enhancement.

For Device C the aspect ratio of the corrugation is larger than for Device B ($r_{h,C} = h_B/\Lambda_B = 0.24$ *versus* $r_{h,B} = 0.07$) and Bragg scattering effects are more pronounced for this device. Figures 3(e) and 3(f) show the angular resolved emission spectrum for Device C. The presence of an intense emission peak in forward direction ($k_x = 0$) confirms that the forward luminance is indeed strongly enhanced with respect to the planar reference device. Moreover, as the eye luminosity function is taken into account when calculating the luminance, the blue-shift of the emission with respect to the planar reference leads to a further increase in forward luminance. Apart from the intense peak at $k_x = 0$, the absence of the typical radiative cavity mode is the most prominent feature of this spectrum.

Hauss *et al.* [34] observed a reduction of emission in a corrugated bottom-emitting OLED due to a more prominent transfer of light intensity from the air cone into wave-guided modes in comparison to the reverse scattering of guided modes into the air cone. However, their approach cannot account for the absence of the fundamental cavity mode in our corrugated microcavity top-emitting OLEDs nor for the observed bending of the dispersion relations. Hence, the emission from Device C cannot be understood simply as the emission of a planar microcavity with superposed Bragg scattering. The weak perturbation approach previously discussed by Hauss *et al.* [34] and Fuchs *et al.* [28] does not suffice to describe these experimental data, despite the fact that the previously mentioned thickness criterion $h_C/d_{\mathrm{opt}} = 0.33 < 1$ holds. This thickness criterion was originally derived for weak optical microcavities of dielectric media excluding metals within the optical microcavity [33]. The extraordinary radiation patterns are thus attributed to the presence of metals within the top-emitting OLEDs and the corresponding increased microcavity effect, indicating the failure of the perturbation model even at a lower h_C/d_{opt} around 0.24.

To gain further insight into the scattering process within strong microcavities with sub-μm corrugation, we consider propagating electromagnetic plane waves $\vec{E}(\vec{r}) = \vec{E}_0 \mathrm{e}^{\imath(k_x x + k_z z)}$ with in-plane wavenumbers $k_x < k_0$, i.e. waves within the outcoupling cone of the microcavity (x-direction). The time dependent part $\mathrm{e}^{-\imath\omega t}$ is dropped for sake of simplicity. As these waves are radiative, the amplitude E_0 decreases as the wave propagates. Therefore, the in-plane wavenumber can be substituted by a complex quantity, i.e. $\hat{k}_x = k_x^{'} + \imath k_x^{''}$. Fourier transformation of $\vec{E}(\vec{r})$

#197952 - $15.00 USD Received 18 Sep 2013; revised 28 Nov 2013; accepted 19 Dec 2013; published 25 Mar 2014

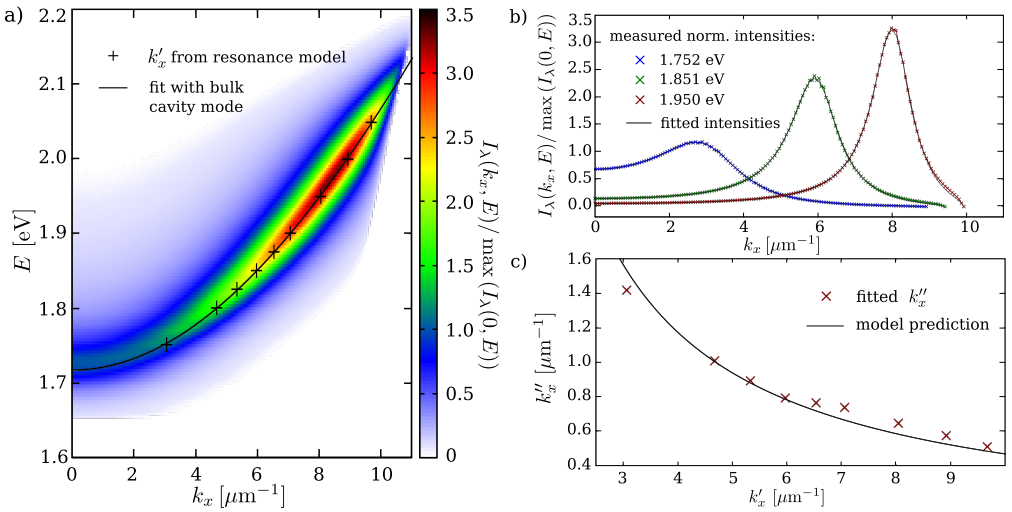

Fig. 5. (a) Simulated normalized spectral radiant intensity for the planar reference (Device A). The fitted positions $k_x^{'}$ of the resonance are highlighted by black crosses. The positions match the dispersion relation for an optical waveguide within an dielectric slab (black line). (b) Spectra from (a) at fixed energies of 1.752 eV, 1.851 eV, and 1.95 eV with the corresponding intensity of the fitted resonance. (c) Dependence of the damping coefficient $k_x^{''}$ on the resonance position $k_x^{'}$. The dependence predicted by the model is fitted to the data (black line).

then leads to a Lorentz-like resonance expression for the field as a function of the in-plane wavenumber

$$E(k_x) = E_0 \left(\frac{e^{-\imath\phi}}{k_x^{'} - k_x + ik_x^{''}} + \frac{e^{\imath\phi}}{k_x^{'} + k_x - ik_x^{''}} \right). \tag{2}$$

This expression describes the field profile as a damped resonance (damping coefficient $k_x^{''}$ and position of center $k_x^{'}$) of the optical microcavity that propagates while gathering up phase ϕ. The field amplitude expression obtained in this way respects causality of mode propagation in real space indicated by the correct parity for in-plane wavenumbers k_x. The imaginary part of the wavenumber $k_x^{''}$ represents a damping coefficient and can be related to the reflection coefficients r of the top "+" and bottom "-" electrode of the microcavity through

$$r_+ r_- = \exp\{-2d_{\text{opt}} k_x^{''} \tan\theta\}. \tag{3}$$

Here, d_{opt} describes the total optical thickness of the microcavity. Furthermore, the reflection coefficients take into account the phase shift originating from $k_x^{'}$ for the projected in-plane propagation with an angle θ. The complex part of the wavenumber $k_x^{''}$ thus depends directly on the position $k_x^{'}$ and on the reflectivity of the microcavity. The description of optical modes as resonances also holds for planar structures. Therefore, we fit the simulated spectral radiant intensity of the planar reference device with one resonance function of the type described in Eq. (2). The results are summarized in Fig. 5. Figure 5(a) shows the simulated spectral radiant intensity for a planar device structure (Device A). At the highlighted energies we applied a fit of the spectra with one resonance function. The fitted resonance positions in Fig. 5(a) agree with the simulated spectra, thus showing that Eq. (2) can be used to determine the angular dispersion of the outcoupled microcavity mode. Furthermore, Fig. 5(b) compares the simulated emission to

#197952 - $15.00 USD Received 18 Sep 2013; revised 28 Nov 2013; accepted 19 Dec 2013; published 25 Mar 2014

the fitted intensities for three different energies from Fig. 5(a). The applied model fits the emission intensity very well, further validating the theoretical approach. In Fig. 5(c) we analyze the dependence of the imaginary part $k_x^{''}$ of the wavenumber on the real part $k_x^{'}$ for the fitted spectrum of the planar microcavity. We notice good agreement between the theoretically predicted properties and the fitted values in the range from $1.41\,\mu\mathrm{m}^{-1}$ to $0.51\,\mu\mathrm{m}^{-1}$, even though the values obtained with Eq. (3) are based on energy-independent reflection coefficients. Estimating values for $k_x^{''}$ from reflection coefficients obtained by transfer-matrix approach yields in damping coefficients in the range from $0.75\,\mu\mathrm{m}^{-1}$ to $0.34\,\mu\mathrm{m}^{-1}$, which are in the same order of magnitude as the values obtained from the fit in Fig. 5(c). Therefore, the radiation from the optical microcavity of the OLEDs is characterized by large damping coefficients $k_x^{''}$, restricting the propagation length along the microcavity to only a few wevelengths. This corresponds to a low quality factor microcavity.

Due to Bragg scattering at the corrugated structure within the microcavity, several resonances (Eq. (2)) can interfere constructively or destructively so that the scattering amplitude can deviate from the case of weak perturbation discussed above, in particular, where several (scattered) modes take the same values for wavenumber and photon energy. Fig. 6(a) shows the measured s-polarized angular resolved emission of Device C at a fixed photon energy of 1.755 eV (corresponding to 705 nm, c.f. Fig. 3(c)). For this photon energy, the change of intensity with angle cannot be described by the simple additive superposition of radiative and scattered modes. Instead, the data were fitted with three interfering resonances, each parametrized according to Eq. (2). We emphasize that we only need to supply the number of resonances for the fitting. All other parameters of the field components are found by numerical minimization of the difference between calculation and experimental data, starting from random numbers. The convergence of such a minimization process is mostly determined by the number of modes involved. The best fit was achieved by assuming that these number of resonances equals the number of modes predicted to be at this particular photon energy inside the air cone (Bragg scattered modes and the microcavity mode) when using the weak perturbation approach described before. For a photon energy of 1.755 eV, this is the radiative cavity mode interfering with the negative first order Bragg scattered radiative cavity mode and with the first order Bragg scattered WGs1 mode. The fit yields the following angular positions $k_{x,i}^{'}$ for the three resonances: $k_{x,1}^{'} = 2.53\,\mu\mathrm{m}^{-1}$, $k_{x,2}^{'} = 3.92\,\mu\mathrm{m}^{-1}$, and $k_{x,3}^{'} = 6.64\,\mu\mathrm{m}^{-1}$. The individual intensity of each of these resonances and their interference (i.e. the intensity of the complex sum) are shown in Fig. 6(a). It can be seen that the complex sum yields an excellent agreement with the measured data. By analyzing the amplitude and phase profiles of the three resonances, we find that Resonance 1 interferes destructively with the other two resonances. More specifically, the fit at 1.755 eV (Fig. 6(a)) obtains phase angles of $\phi_1 = 1.49\,\pi$, $\phi_2 = 0.95\,\pi$ and $\phi_3 = 1.15\,\pi$, revealing a pronounced phase shift between the first and second mode ($\Delta\phi > \pi/2$), but constructive interference for the second and third resonance ($\Delta\phi \approx 0.2\pi$). The destructive interference of propagating Bragg scattered modes leads to a reduction of the emitted light at wavenumbers around $k_x = 2.05\,\mu\mathrm{m}^{-1}$. The imaginary components of the wavenumbers $k_{x,i}^{''}$ were fitted to $k_{x,1}^{''} = 1.22\,\mu\mathrm{m}$, $k_{x,2}^{''} = 0.96\,\mu\mathrm{m}$ and $k_{x,3}^{''} = 1.57\,\mu\mathrm{m}$. These values are in the expected range for the damping constants. However, they no longer follow the simple relation shown in Fig. 5(c) as the periodic structure strongly changes the reflectivity of the microcavity at wavenumbers and energies corresponding to Bragg scattering angles.

The amplitudes of the modes occurring in Fig 6(a) follow our expectations, as the calculated power dissipation spectra showed larger intensities for the waveguided modes than for the radiative cavity mode. Furthermore, the amplitude of a mode will be decreased by the Bragg scattering process as the scattering efficiency of the structure is smaller than unity.

#197952 - $15.00 USD Received 18 Sep 2013; revised 28 Nov 2013; accepted 19 Dec 2013; published 25 Mar 2014

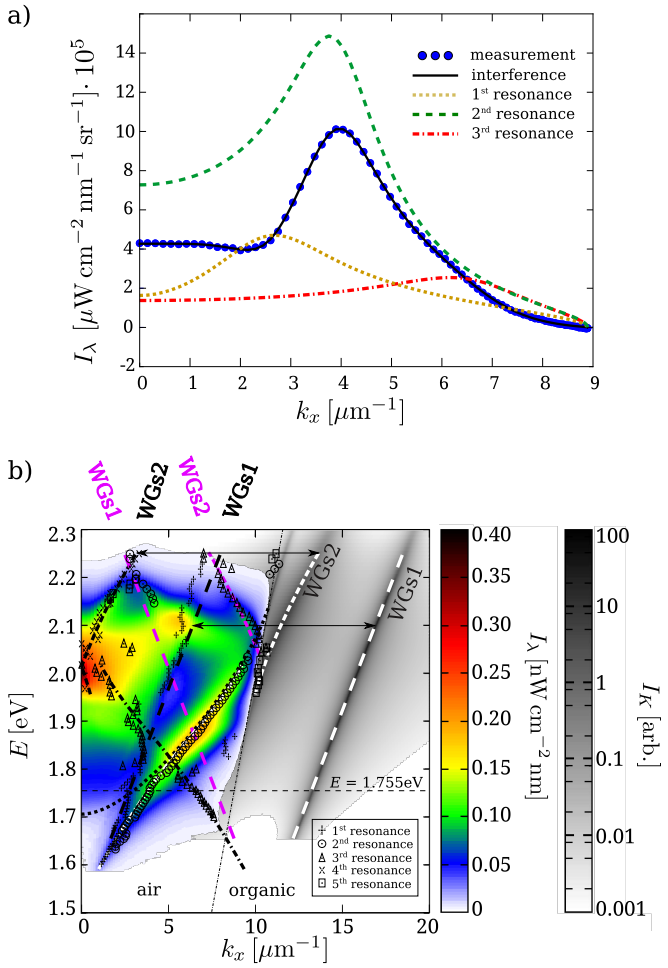

Fig. 6. (a) Measured s-polarized spectral radiant intensity of Device C from Fig. 3(e) for a photon energy of 1.755 eV (corresponding to a wavelength of 705 nm) along with a fit to the data based on the interference of three resonances, each described according to Eq. (2). The interference corresponds to the complex sum of the three resonances, the k_x dependence of the individual resonance is also shown for completeness. (b) Symbols: Center position of resonances fitted to the complete s-polarized angular resolved emission spectrum of Device C. Up to 5 interfering resonances were allowed at each energy. False color scale data to the left of the air light line represents measured angular emission spectra. Grayscale data to the right of the air light represents the calculated power dissipation spectrum. The dotted line indicates the expected dispersion of the radiative cavity mode. The dash-dotted lines represent the dispersion of the coupled cavity and WGs1 mode, and the dashed lines indicate wave-guided modes (WGs1: long-dashed, WGs2: short-dashed).

#197952 - $15.00 USD Received 18 Sep 2013; revised 28 Nov 2013; accepted 19 Dec 2013; published 25 Mar 2014

Finally, this fitting algorithm is applied to the complete spectral range relevant for Device C (photon energies of 1.5-2.3 eV). With respect to the particular photon energy, up to five interfering modes have to be considered in the fitting algorithm in order to describe the measured interference pattern. The symbols in Fig. 6(b) show the position $k'_{x,i}$ of the resonances obtained from the fit at each photon energy. The data is superimposed with the measured angular resolved spectrum and the calculated power dissipation spectrum. For all emitted wavelengths we observe destructive interference between the outcoupled cavity mode and the first Bragg scattered copy of the waveguided mode (WGs1), propagating with refractive group index $n_g = 2.08$. This reduction in emitted light leads to the lower EQE of Device C compared with the other devices. Further, the high forward luminance of Device C can be assigned to the interference of the first Bragg scattered modes of the WGs2 mode with $n_g = 2.48$ at normal emission angle $k_x = 0$. We observe pronounced destructive interference in the wavenumber interval of $k_x = 2.07$ to $3.81\,\mu\mathrm{m}^{-1}$ and in an energy range of $E = 1.7$ to 1.85 eV. The modes involved are the second order cavity mode (normally the emissive mode) and the first order Bragg scattered waveguided mode (WGs1). The mode coupling leads to the complete disappearance of the cavity mode at small emission angles and thus results in an additional reduction in emission. The dispersion of the coupled mode can be observed in the spectra, highlighted by a white dash-dotted line in Fig. 6(b). Furthermore, the coupled mode is also Bragg scattered and the first scattered mode can be identified in the measured spectra (black dash-dotted line in Fig. 6(b)).

4. Conclusion

In summary, we have demonstrated that the outcoupling efficiency for optically optimized top-emitting OLEDs can be further enhanced by introducing periodically corrugated substrates that cause Bragg scattering of waveguided modes normally confined within the OLED stack. Detailed investigations on the angular resolved emission patterns have allowed to assign the origin of the different enhancement effects for different grating periods. For the corrugated devices we found additional emission by Bragg scattered waveguided modes. Further, very high forward luminance for a corrugated device compared to the planar reference was achieved by introducing a grating with 0.6 μm period. Directed emission of OLEDs might be beneficial for many applications, e.g. spot lights or signaling. In this device we also found evidence for destructive interference and mode coupling that reduces the angle-integrated emission intensity. These additional effects arise from interference of resonant modes of the microcavity. Future studies will focus on optimizing the corrugation pattern further, avoiding destructive mode interference and improving the efficiency enhancement beyond the 13 % shown here.

Acknowledgments

This work was funded by the European Social Fund and the Free State of Saxony through the OrganoMechanics project, and by the AIF/BMWi in the framework IGF under contract no. GF-11/05 resp. AiF-Nr. 16784 BR (project LipsOLED). Support from the excellence cluster cfaed is gratefully acknowledged. We acknowledge support by the German Research Foundation and the Open Access Publication Funds of the TU Dresden.

#197952 - $15.00 USD Received 18 Sep 2013; revised 28 Nov 2013; accepted 19 Dec 2013; published 25 Mar 2014